Chinese Chemical Letters 37 (2026) 111970

Contents lists available at ScienceDirect

Chinese Chemical Letters

journal homepage: www.elsevier.com/locate/cclet

NIR-activated phototherapy for targeted therapy of MRSA-induced wound infection and pneumonia

Qijia Sun[a], Wenhai Lin[b], Ranwei Li[c], Qingxuan Li[a], Ke Wang[a,*], Zhigang Xie[d,*]

[a] Department of Respiratory and Critical Care Medicine, The Second Hospital of Jilin University, Changchun 130041, China
[b] Biomedical Polymers Laboratory, College of Chemistry, Chemical Engineering and Materials Science and State Key Laboratory of Radiation Medicine and Protection, Soochow University, Suzhou 215123, China
[c] Department of Urology, The Second Hospital of Jilin University, Changchun 130041, China
[d] State Key Laboratory of Polymer Science and Technology, Changchun Institute of Applied Chemistry, Chinese Academy of Sciences, Changchun 130022, China

ARTICLE INFO

Article history:
Received 19 August 2025
Revised 11 October 2025
Accepted 14 October 2025
Available online 15 October 2025

Keywords:
Methicillin resistant *Staphylococcus aureus*
Photothermal therapy
Photodynamic therapy
Diabetic wound
Pneumonia

ABSTRACT

The multidrug resistance and robust biofilm-forming capacity of methicillin-resistant *Staphylococcus aureus* (MRSA) present significant challenges to clinical therapy, underscoring the urgent need for the effective antibacterial strategies. While synergistic approaches combining photodynamic therapy (PDT) and photothermal therapy (PTT) exhibit considerable promise, their efficacy is frequently constrained by limitations in targeted delivery to bacteria and biofilms. This study developed a multifunctional nanoparticle (BDPV) through the conjugation of vancomycin (VAN) with distearoylphosphatidylethanolamine-polyethylene glycol 2000 (DSPE-PEG_{2000}) and the encapsulation of a 4,4-difluoro-4-bora-3a,4a-diaza-*s*-indacene derivative (BODIPY) possessing both photodynamic and photothermal properties. BDPV employs a dual-targeting mechanism: (1) VAN enables specific targeting of peptidoglycan in the bacterial cell wall; (2) under the conditions of infection microenvironments, BODIPY undergoes protonation, resulting in charge reversal from negative to positive, thereby enhancing electrostatic interaction to bacteria. Upon irradiation with the near-infrared (NIR) laser, BDPV synergistically generates potent photodynamic and photothermal antibacterial effects, which facilitates highly efficient targeting and effective eradication of drug-resistant bacterial infections. Furthermore, BDPV demonstrated remarkable therapeutic efficacy in both deep-tissue infection models (pneumonia) and superficial infection models (skin wounds). This strategy provides a promising new approach for overcoming drug-resistant bacterial infections and treating associated biofilm-related diseases.

© 2026 Published by Elsevier B.V. on behalf of Chinese Chemical Society and Institute of Materia Medica, Chinese Academy of Medical Sciences.

Bacterial pneumonia represents a major global health threat, associated with persistently high morbidity and mortality rates [1]. Within this challenging context, methicillin-resistant *Staphylococcus aureus* (MRSA) emerges as a significant pathogen, presenting a formidable challenge [2]. The emergence and widespread dissemination of MRSA have substantially complicated the treatment of infectious diseases [3,4]. MRSA is not only highly toxic and pathogenic in its own right, but its dense biofilm structure is also a major obstacle to treatment [5,6]. In clinical practice, although antibiotic therapy remains the conventional approach, the presence of biofilms significantly compromises its bactericidal efficacy. Bacteria encased within the dense extracellular polymeric substance (EPS) matrix of a biofilm can exhibit antibiotic resistance levels 10–1000 times higher than their planktonic counterparts [7,8]. This type of deep resistance mediated by biofilms makes the eradication of MRSA infections, especially those related to biofilms, extremely difficult [9–12]. Consequently, the development of alternative antimicrobial strategies capable of effectively overcoming the biofilm barrier is imperative.

Phototherapy has gained widespread attention as an effective strategy against bacterial infections due to its controllability in time and space, minimal invasiveness, and the ability to circumvent bacterial resistance [13–16]. Phototherapy includes photothermal therapy (PTT) and photodynamic therapy (PDT). Traditional PTT suffers from insufficient precise temperature control, inevitably causing thermal damage to healthy tissues [17–19]. PDT works by generating reactive oxygen species (ROS) through photosensitizers (PSs) [20]. ROS are highly reactive and have a short half-life, thus affecting only cells in the immediate vicinity of the generation area, and causing minimal side effects [21,22]. However,

* Corresponding authors.
E-mail addresses: wke@jlu.edu.cn (K. Wang), xiez@ciac.ac.cn (Z. Xie).

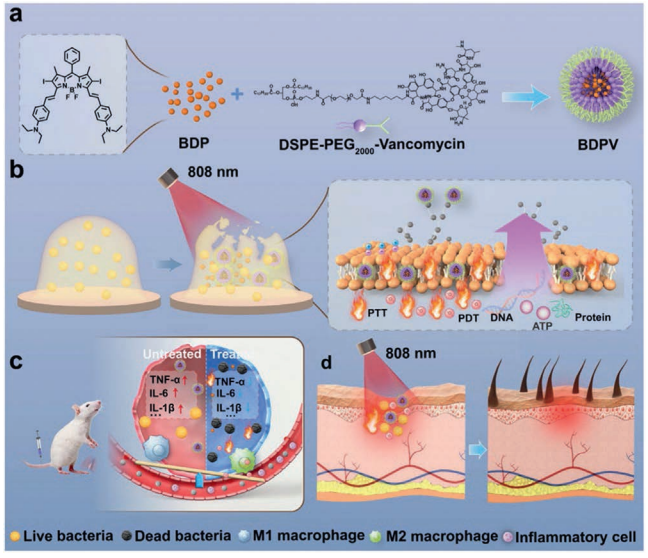
https://doi.org/10.1016/j.cclet.2025.111970
1001-8417/© 2026 Published by Elsevier B.V. on behalf of Chinese Chemical Society and Institute of Materia Medica, Chinese Academy of Medical Sciences.

the reduced membrane permeability of drug-resistant bacteria hinders the entry of ROS and weakens the destruction of intracellular structures, ultimately affecting the bactericidal effect [23–26]. Given the limitations of PTT and PDT, the combined strategy shows significant synergistic advantages [27–30]. On one hand, the inherent antibacterial activity of PDT helps lower the temperature required for PTT to achieve effective bactericidal effects, thereby reducing the risk of thermal damage [31–33]. Despite the significant advantages of the combined therapy, phototherapy antibacterial strategies still face challenges, such as the limited penetration depth of short-wavelength light into biological tissues and the lack of targeting leading to insufficient enrichment at the infection site [34,35]. Therefore, the development of intelligent delivery systems that integrate active targeting, microenvironmental responsiveness, and dual-mode bactericidal effects is imperative [36].

Herein, this study constructed vancomycin (VAN)-functionalized BDVP. VAN was covalently conjugated to the terminal of the distearoylphosphatidylethanolamine-polyethylene glycol 2000 (DSPE-PEG_{2000}) carrier *via* an amide bond, endowing nanoparticles with the ability to specifically recognize D-Ala-D-Ala peptidoglycan on the MRSA cell wall. Meanwhile, a 4,4-difluoro-4-bora-3a,4a-diaza-*s*-indacene derivative (BODIPY) modified by tertiary amines was used as PSs. This PS undergoes protonation in the acidic microenvironment of biofilms, inducing a charge reversal from negative to positive on the surface, thereby enhancing the affinity with negatively charged bacteria through electrostatic attraction. Under 808 nm laser irradiation, the BODIPY simultaneously mediates the generation of singlet oxygen ($^1O_2$) and local temperature rise effects, achieving dual-mode synergistic bactericidal effects of physical membrane disruption and chemical oxidative damage (Scheme 1). Ultimately, an anti-MRSA strategy was established, which realizes ligand-mediated targeted accumulation, microenvironment-responsive charge reversal, and near-infrared (NIR)-triggered synergistic bactericidal effects. This strategy provides a new approach to overcome biofilm-related drug-resistant bacterial infections.

Scheme 1 details the preparation procedure for BDPV. Specifically, BODIPY was successfully synthesized based on the previous work. Subsequently, VAN was covalently conjugated to the DSPE-PEG_{2000} carrier molecule *via* an amide coupling reaction, followed by encapsulating the BODIPY. The stable nanoparticles (BDPV) were ultimately prepared by using the nanoprecipitation method. Notably, BDPV exhibits broad NIR absorption spanning 650–850 nm (Fig. 1a). Transmission electron microscopy (TEM) characterization demonstrated that the resulting BDPV possess a uniform spherical morphology (Fig. 1b). Dynamic light scattering (DLS) measurements determined a hydrodynamic diameter of 150.67 ± 2.43 nm (Fig. 1b). The colloidal stability of BDPV was systematically evaluated. After 14 days of storage at 4 °C, DLS analysis showed no significant changes in hydrodynamic diameter or polydispersity index (PDI) values (Fig. 1c), confirming good long-term stability in aqueous media. Additionally, stability testing under physiological conditions (0.9 % NaCl solution) over 48 h revealed no significant alterations in particle size or PDI (Fig. S1 in Supporting information), further verifying robust salt stability. As a control, BODIPY nanoparticle (BDP) obtained by self-assembly in the absence of DSPE-PEG_{2000}. Zeta potential analysis indicated a surface potential of -12.6 ± 1.04 mV for BDP (Fig. 1d). Following functionalization, BDPV exhibited a decreased potential of -20 ± 1.96 mV, electrochemically confirming successful DSPE-PEG_{2000}-VAN coating.

To systematically evaluate the PDT potential of BDPV, 1,3-diphenylisobenzofuran (DPBF) was employed as a trapping agent to assess $^1O_2$ generation capacity. As shown in Fig. 1e, the absorption intensity of DPBF showed no significant change within 60 s under 808 nm laser irradiation (0.3 W/cm²). The absorbance in the presence of BDPV exhibited a time-dependent attenuation (Fig. 1e and Fig. S2 in Supporting information), confirming that BDPV could generate ROS. Given that the bacterial infection microenvironment is usually slightly acidic [37], we further investigated the effect of pH value on the photodynamic activities of BDPV [38]. As demonstrated in Fig. 1e, the decay rate of absorbance under acidic conditions further decreased compared to that in the neutral environment. This phenomenon is attributed to the protonation-induced charge recombination of BDP under acidic



Scheme 1. Schematic diagram of the preparation, antibacterial mechanism and therapeutic effect of BDPV nanoparticles. (a) Schematic diagram of BDPV preparation and performance. (b) The synergistic mechanism of BDPV(+) against MRSA infection. Applications of BDPV(+) in the treatment of (c) bacterial pneumonia and (d) bacteria-infected wound healing caused by MRSA.

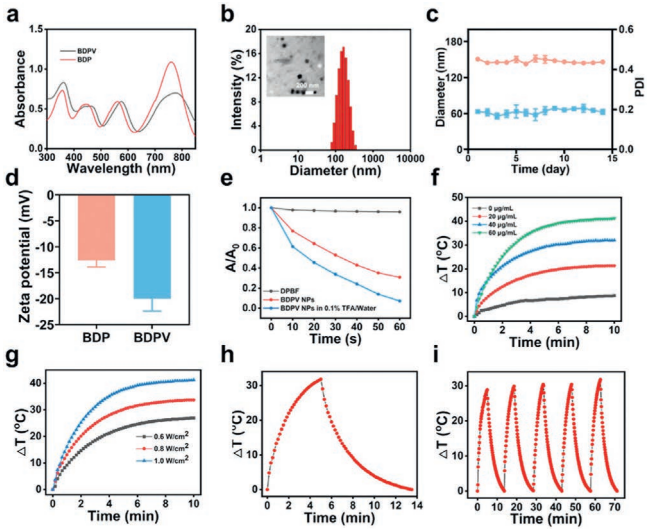


Fig. 1. The relevant characteristics of BDPV. (a) Absorption spectra of BDP in *N*,*N*-dimethylformamide (DMF) and BDPV in water. (b) Size distribution of BDPV characterized by DLS. Inset: TEM image of BDPV. Scale bar: 200 nm. (c) Changes in particle size and PDI of BDPV in deionized water. (d) Zeta potential of BDP and BDPV nanoparticles. Data are presented as mean ± standard deviation (SD) ($n = 3$). (e) $^1O_2$ generation of BDPV trapped with DPBF in deionized water (with or without 0.1 % TFA) under 808 nm laser irradiation. (f) Temperature rising of BDPV at different concentrations upon laser irradiation (0.3 W/cm²). (g) Temperature changes of BDPV exposed to an 808 nm laser with various power densities. (h) Photothermal effect of BDPV under irradiation and the laser turned off after 5 min. (i) Temperature changes of BDPV during 5 cycles of heating and cooling.

conditions, which enhances photosensitization efficiency. This result indicates that BDPV selectively enhances the ability to generate $^1O_2$ in the microenvironment of the infection site.

Photothermal conversion efficiency (PCE) is a critical parameter for evaluating the bactericidal performance of photothermal agents. Accordingly, we systematically investigated the photothermal behaviors of BDPV under laser irradiation. As shown in Fig. 1f, the temperature increasing (ΔT) was significantly positively correlated with the concentration of BDPV. When the concentration of BDPV reached 60 μg/mL, ΔT increased to 43.7 °C, significantly higher than the temperature rise of deionized water. In addition, ΔT increased progressively with higher laser power densities at a fixed concentration (60 μg/mL), confirming the controllable photothermal conversion performance (Fig. 1g). Based on the cooling curve (Fig. 1h and Fig. S3 in Supporting information), the photothermal conversion efficiency (η) of BDPV was calculated to be 35.9 %, surpassing that of indocyanine green (ICG, $\eta \approx 20$ %). Notably, BDPV maintained stable temperature increasing throughout five heating-cooling cycles (Fig. 1i), demonstrating robust photothermal stability.

MRSA poses a significant threat to global health due to its high drug resistance and pathogenicity [39]. Microbroth dilution assays determined the minimum inhibitory concentration (MIC) of BDPV against MRSA to be 80 μg/mL (Fig. S4 in Supporting information), achieving 91.7 % of bacterial inhibition. Subsequently, we further compared the antibacterial properties of VAN group, DSPE-PEG_{2000}-VAN (PEG-VAN) group, BDP + laser (BDP(+)) group, BDPV group, and BDPV + laser (BDPV(+)) group. To visually assess the antibacterial properties, the mixed solutions after different treatments were spread on agar plates (Figs. 2a and b), and it could be observed that the phosphate buffered saline (PBS) group had abundant colonies covering the entire agar plate, while the BDPV(+) group had almost no colony formation on the plate, indicating the antibacterial effect. It is noteworthy that compared with the BDP(+) group containing only PS, the antibacterial effect of BDPV(+) was obvious, which was attributed to the fact that VAN first binds to the peptidoglycan precursor of the cell wall and then combines with the cell membrane. At the same time, live/dead staining was performed to evaluate bacterial viability. MRSA in the control group, PEG-VAN group, and BDPV group showed strong green fluorescence of viable bacteria (Figs. 2c and d). In contrast, the MRSA in the BDPV group showed strong red fluorescence, validating that BDPV has significant antibacterial efficacy under NIR laser irradiation.

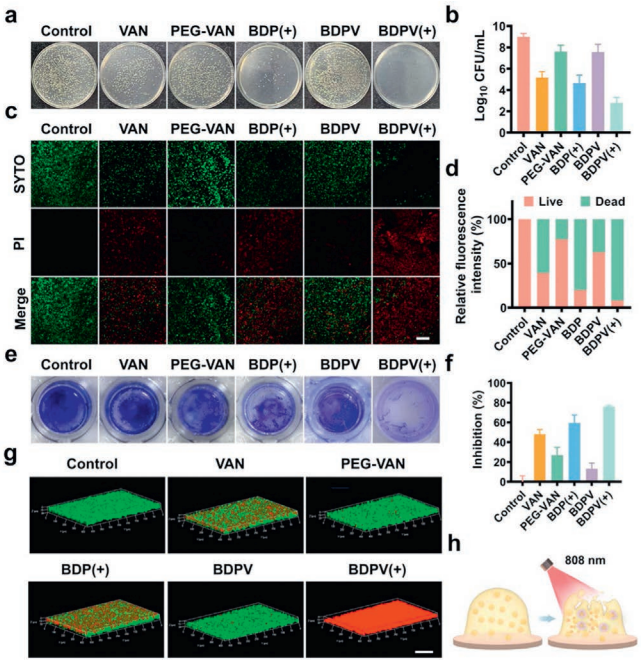


Fig. 2. The *in vitro* antibacterial properties of BDPV. (a) Photographs of representative agar plates after different treatments. (b) Quantitative results of agar plates after different treatments. (c, d) Live/dead staining images and quantitative analysis of MRSA after different treatments. SYTO, green fluorescent nucleic acid stain; PI, propidium iodide. Scale bar: 100 μm. (e) Images of crystal violet staining after different treatments. (f) Biofilm inhibition rate by different treatment groups. (g) 3D biofilm structure of different treatment groups. (h) Diagram of the mechanism of biofilm destruction. Scale bar: 100 nm. Data are presented as mean ± SD ($n = 3$).

Bacterial biofilms create physical barriers that compromise antibiotic penetration [40–42]. This physical barrier can reduce the efficiency of antibiotic penetration and significantly enhance the immune evasion ability of bacteria [43,44]. To address this clinical issue, this study systematically evaluated the intervention effect of BDPV on MRSA biofilms. The results of crystal violet staining analysis (Figs. 2e and f, Fig. S5 in Supporting information) showed that compared with the control group, the free VAN and BDP(+) groups had biofilm clearance rates of 48.1 % and 59.2 % respectively, while the BDPV(+) group achieved a clearance rate of 75.9 %. Further, the destruction of mature biofilms was evaluated by confocal laser scanning microscopy (CLSM) (Figs. 2g and h). The bacteria in the PBS group showed strong green fluorescence of live bacteria, while the mixed red and green fluorescence were observed in the VAN group, PEG-VAN group and BDP(+) group. There was weak green fluorescence and obvious red fluorescence of dead bacteria for the treatment of BDPV(+). BDPV(+) exhibited a significant synergistic effect based on three aspects: (1) VAN enhanced the bacterial surface adhesion, promoting the enrichment of nanoparticles at the local site; (2) the photothermal effect promoted the penetration; (3) the charge inversion caused by the acidic environment further increased the local enrichment of BDP. In conclusion, BDPV(+) achieved effective inhibition and clearance of the biological membranes through a triple synergistic mechanism: targeted penetration, photodynamic-photothermal synergy and matrix degradation.

To deeply elucidate the antibacterial mechanism of BDPV under irradiation, the generation of ROS within the MRSA biofilm was first detected by using the 2′,7′-dichlorodihydrofluorescein diacetate (DCFH-DA) fluorescence probe. The results showed that significant green fluorescence was observed in both the BDP(+) group and the BDPV(+) group with laser irradiation, indicating the generation of ROS, while no fluorescence signals were detected in the other control groups (Fig. S6 in Supporting information). Secondly, the effects of different treatments on the morphology of MRSA were observed by scanning electron microscopy (SEM). It was observed that the bacterial morphology in the control group was regular and intact, while there was obvious wrinkling deformation accompanied by the leakage of cellular contents in the BDP(+) and BDPV(+) groups (Fig. S7 in Supporting information). To further evaluate the integrity of the cell membrane, we measured the intracellular ATP level and protein leakage of the bacteria [45,46]. The data showed that compared with other treatment groups, the intracellular ATP level in the BDPV combined with laser irradiation was significantly reduced and its protein leakage was the most severe (Fig. S8 in Supporting information). These results indicate that BDPV can accumulate at the infection site and cause the denaturation of bacterial DNA and proteins under laser irradiation, and ultimately severely damage the cell membrane.

We further evaluated the *in vivo* therapeutic efficacy of BDPV-mediated synergistic therapy by using an MRSA-infected wound model in aged diabetic mice induced by streptozotocin (STZ) (Fig. 3a). All animal experiments have been approved by the Animal Welfare and Ethics Committee of Jilin University (approval No. KT202408194), and were conducted in strict accordance with the guidelines for the care and use of laboratory animals issued by

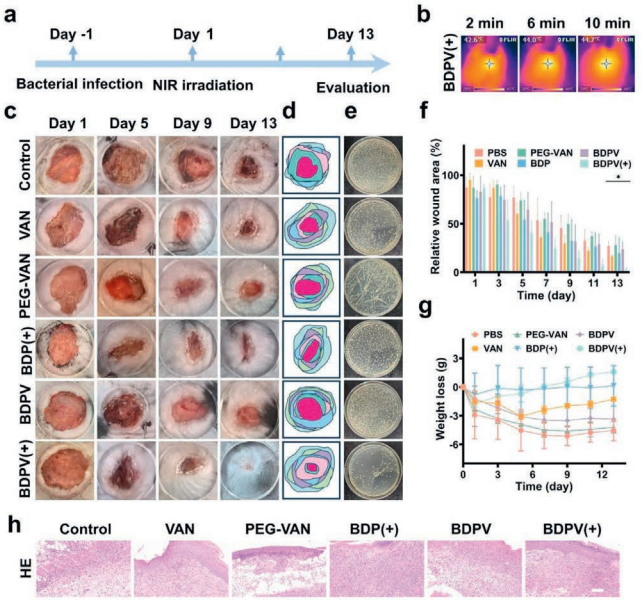


Fig. 3. The antibacterial effect of BDPV(+) in the wound infection model of diabetic mice. (a) Establishment of wound infection model and treatment plan. (b) The change in wound temperature after laser irradiation. (c) The healing status of the wound at different time points. (d) Wound images on different dates during treatment. (e) Agar plates of residual bacteria on wounds. (f) Diagram of wound healing process. (g) The weight loss of each group during the treatment period. Data are presented as mean ± SD ($n = 3$). (h) Histological examination of HE. Scale bar: 100 nm.

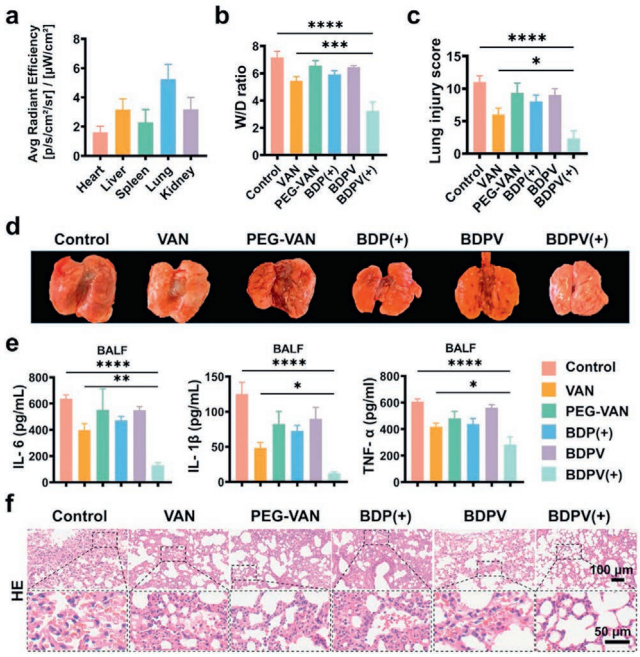


Fig. 4. Antimicrobial efficacy of BDPV(+) in a model of bacterial pneumonia. (a) Fluorescence distribution in major organs 24 h after drug injection. (b) Ratio of lung wet weight to dry weight in different treatment groups. (c) Lung tissue injury scores of different groups. (d) Photographs of representative lung tissue from different treatment groups. (e) Cytokine levels of IL-6, IL-1β and TNF-α in BALF of mice in different treatment groups. (f) HE of lungs tissue from various groups. Data are presented as mean ± SD ($n = 3$). $^{*}P < 0.05$, $^{**}P < 0.01$, $^{***}P < 0.001$, $^{****}P < 0.0001$.

the National Institutes of Health (NIH publication number. 85–23, Rev. 1985). During the treatment process, infrared thermography showed significant differences in temperature changes of wound. Consistent with expectations, the temperature in the control group did not increase significantly. In contrast, the temperature in the BDPV(+) group rose rapidly and remained above 42 °C (Fig. 3b and Fig. S9 in Supporting information), indicating an effective photothermal effect. The wound healing after local treatment further confirmed the efficacy of BDPV. As shown in Fig. 3c and Fig. S10 (Supporting information), the BDPV(+) group demonstrated the most accelerated healing, achieving 94.8 % wound closure by day 13, significantly superior to the control group (73.0 %) (Figs. 3d and f). Bacterial smears of wound tissues also revealed substantially reduced bacterial loads in the BDPV(+) group (Fig. 3e). After MRSA infection, mice in all groups exhibited obvious weight loss (Fig. 3g). BDPV(+) group displayed initial weight loss followed by recovery, indicating more effective control of infection. Antibacterial treatment is key to promoting wound healing by eliminating pathogenic bacteria and shortening the inflammatory stage [47,48]. The histological analysis of the wound tissue (hematoxylin and eosin staining (HE), Masson staining) provided deeper evidence (Fig. 3h and Fig. S11 in Supporting information). Compared with other groups, the BDPV(+) group had the least inflammatory cell infiltration and the most abundant collagen fiber deposition. Given that the formation of new blood vessels is a key indicator of wound remodeling [49,50], we evaluated the density of angiogenesis by immunofluorescence staining of platelet endothelial cell adhesion molecule 1 (CD31). The results showed that the intensity of red signals was strongest with the high distribution density in the BDPV(+) group (Fig. S11), indicating that the wound microenvironment in the BDPV(+) group was more conducive to regeneration and repair. In conclusion, BDPV combined with laser irradiation can effectively combat MRSA infection and significantly accelerate the healing process of infected wounds by promoting tissue repair, demonstrating great clinical application potential.

We further explored its targeting ability of BDPV *in vivo*. A mouse pneumonia model was established by intratracheal instillation of an MRSA bacterial suspension. The bacterial targeting capability of DSPE-PEG$_{2000}$-VAN was then assessed through tail vein injection of PEG-VAN@IR780. We dynamically monitored the fluorescence intensity of major organs through the *in vivo* imaging system (IVIS). The results of *in vivo* and *ex vivo* imaging (Fig. S12 in Supporting information) were consistent, showing that the BDPV could significantly accumulate in the lungs over time, reaching a peak at 24 h after injection. The fluorescence distribution in major organs at 24 h after injection (Fig. 4a) further confirmed that the accumulation in the lungs was more than that in the liver and kidneys. These results clearly demonstrated that BDPV could achieve efficient pulmonary targeting location, laying the foundation for the treatment of pulmonary infections.

We next evaluated the therapeutic efficacy of BDPV with irradiation in a murine model of acute MRSA-induced pneumonia. During the treatment process, the thermal imaging instrument monitoring showed that the lung temperature of the BDPV(+) group mice continued to rise, reaching 42.5 °C after 10 min of irradiation. In contrast, the temperature increase in the control group under the same irradiation conditions was not significant (Fig. S13 in Supporting information). Macroscopic examination of lung tissues post-treatment showed severe congestion and edema in Control, PEG-VAN, and BDPV groups, moderate pathology in VAN and BDP(+) groups, and minimal pathological changes in the BDPV(+) group (Fig. 4d). The lung edema degree obtained by calculating the wet/dry weight ratio of lung tissue showed that the ratio in the BDPV(+) group was the lowest (Fig. 4b), indicating that BDPV with irradiation can effectively alleviate the inflammation and edema caused by lung infection. The colony culture results of lung tissue homogenate directly showed that the colonies grew densely on the agar plates of the control group, while the colonies in the BDPV(+) group significantly decreased

(Fig. S14 in Supporting information). The semi-quantitative analysis (Fig. S14) further confirmed that the bacterial load in the lungs of the BDPV(+) group was significantly lower than that of all other experimental groups. Survival rate monitoring provided the most critical evidence of efficacy. The survival rate of mice in the control group was only 50%, while that of the BDPV(+) group was as high as 91.7% (Fig. S15 in Supporting information). Overall, the results show that BDPV under irradiation, with its lung-targeted accumulation ability and efficient photodynamic photothermal synergy effect, can effectively kill pathogenic bacteria (MRSA) in the lungs, significantly reduce lung inflammation and edema, and ultimately significantly increase the survival rate of infected mice.

To evaluate the therapeutic efficacy of BDPV-mediated synergistic therapy against pneumonia, we systematically analyzed its impact on pro-inflammatory cytokine expression and immune cell infiltration [51]. Serum and bronchoalveolar lavage fluid (BALF) were collected at the experimental endpoint. Levels of key pro-inflammatory cytokines (interleukin-6 (IL-6), IL-1β, and tumor necrosis factor-α (TNF-α)) were quantified by using enzyme-linked immunosorbent assays (ELISA). As shown in Fig. 4e and Fig. S16 (Supporting information), both serum and BALF exhibited concordant cytokine expression of the significantly elevated levels in controls *versus* markedly suppressed expression across all cytokines in the BDPV(+) group. Given neutrophils serve as primary effector cells in MRSA-induced inflammation [52,53], we evaluated their infiltration by immunofluorescence staining of myeloperoxidase (MPO), a neutrophil-specific marker. The BDPV(+) group displayed the weakest MPO signal intensity in lung tissues compared to other treatments (Fig. S17 in Supporting information), validating the most effective reduction in neutrophil recruitment to infection sites. Visual pathological evidence was provided by the results of HE of lung tissue (Fig. 4f), which showed that the obvious congestion and oedema of the alveolar walls and a large number of inflammatory cell infiltration in the alveolar lumen for the control, PEG-VAN and BDPV groups. In contrast, the lung tissue of the BDPV(+) group was relatively intact and clear, with only a small amount of inflammatory cell infiltration. The BDPV(+) treatment had significantly less lung tissue damage than all other groups, as further quantified by the combined pathological damage scores (Fig. 4c). Analysis of macrophage phenotypes at the site of infection (Fig. S18 in Supporting information) showed that lung tissue in control presented a high density of pro-inflammatory M1 macrophages ($F4/80^+$ $CD11C^+$) and a low density of anti-inflammatory/repairing M2 macrophages ($F4/80^+$ $CD206^+$). The BDPV(+) treatment exhibited significantly reduced M1 macrophage signals and significantly enhanced M2 macrophage signals. Flow analysis accurately quantified the proportion of macrophage subpopulations in the lung tissue (Fig. S18). The percentage of M1-type macrophages in the control group was 1.69 times higher than that in the BDPV(+) group, whereas the highest percentage of M2 macrophages was found in the BDPV(+) group, reaching 2.7 times higher than that in the control group. This result conclusively demonstrates that BDPV combined with laser irradiation effectively promotes macrophage polarisation from pro-inflammatory M1 to anti-inflammatory/restorative M2. BDPV combined with irradiation demonstrates strong anti-inflammatory and immune regulatory capabilities. BDPV can effectively inhibit the release of key pro-inflammatory factors, reduce neutrophil infiltration, alleviate pathological damage to lung tissue, and reverse the pro-inflammatory microenvironment at the infection site.

We systematically evaluated the cytotoxicity and *in vivo* biosafety of BDPV. The cytotoxicity of BDPV was examined by MTT assay on a variety of cell lines, including mouse fibroblasts (L929), mouse embryonic fibroblasts (NIH 3T3), and human non-small cell lung cancer cells (A549). As shown in Fig. S19 (Supporting information), the viability of all cells tested exceeded 80% even at a concentration of 120 μg/mL. This result indicates that BDPV did not exhibit significant cytotoxicity in the therapeutic dose range used in this study. Systemic toxicity was assessed by assaying key biochemical indices in the serum of treated mice. Levels of alanine aminotransferase (ALT), aspartate aminotransferase (AST), blood urea nitrogen (BUN) and creatinine (CREA) did not show significant differences between the groups (Fig. S19), suggesting that BDPV treatment did not cause significant hepatic and renal impairment. Histological analysis of major organs such as heart, liver, spleen, lungs and kidneys were analyzed by HE (Fig. S20 in Supporting information), and no obvious inflammatory lesions and other pathological abnormalities were observed in the organ tissues of all groups. These results proved that the BDPV have good biocompatibility and systematic safety at the current doses in this study.

In summary, the present study successfully reported a multifunctional nanoparticle BDPV, which can achieve efficient targeting and clearance of drug-resistant bacteria through the specific recognition, microenvironment response aggregation, and light-activated synergistic killing simultaneously. BDPV can alleviate excessive inflammation and promote the immune response related to tissue repair, which demonstrated excellent comprehensive therapeutic effects in both deep tissue infections and superficial infections models. This study demonstrated potent therapeutic effects in both deep tissue infection and superficial infection models. This study not only provides a promising phototherapeutic nanoplatform for overcoming bacterial drug resistance and biofilm-associated persistent infections, but also lays an important foundation for the development of the next generation of smart anti-infective drugs by integrating targeting and synergistic therapeutic strategies.

CRediT authorship contribution statement

Qijia Sun: Writing – original draft, Software, Methodology, Investigation, Data curation. **Wenhai Lin:** Resources. **Ranwei Li:** Resources. **Qingxuan Li:** Investigation. **Ke Wang:** Supervision, Resources. **Zhigang Xie:** Supervision, Resources, Conceptualization.

Declaration of competing interest

The authors declare that they have no known competing financial interests or personal relationships that could have appeared to influence the work reported in this paper.

Acknowledgments

This study was supported by Disciplinary Crossing and Integration and innovation project of Norman Bethune Health Science Center of Jilin University (No. 2022JBGS07), Research and Development of Key Medical Technologies of Jilin Science and Technology Department (No. 20240305080YY), Jilin Province Natural Science Foundation - Provincial-Government-Enterprise Joint Fund (Group B) (No. YDZJ202501ZYTS317) and Science and Technology Resource Development in Jilin Province (No. 20250206013ZP).

Supplementary materials

Supplementary material associated with this article can be found, in the online version, at doi:10.1016/j.cclet.2025.111970.

References

[1] W. Jin, L. Liao, T. Qin, et al., Chin. Chem. Lett. 36 (2025) 110920.
[2] J.A. Grousd, H.E. Rich, J.F. Alcorn, Clin. Microbiol. Rev. 32 (2019) e00107–18.
[3] Y. Zhang, Z.T. Jiang, Y. Wang, et al., ACS Nano 18 (2024) 27340–27357.
[4] G.Y.C. Cheung, J.S. Bae, M. Otto, Virulence 12 (2021) 547–569.
[5] K. Tam, V.J. Torres, Microbiol. Spectr. 7 (2019), doi:10.1128/microbiolspec.GPP3-0039-2018.

[6] Z. Li, H. Zhuang, G. Wang, et al., BMC Infect. Dis. 21 (2021) 74.
[7] O. Ciofu, C. Moser, P. Jensen, N. Høiby, Nat. Rev. Microbiol. 20 (2022) 621–635.
[8] Y. Liu, L. Zhang, K. Liu, et al., Chin. Chem. Lett. 35 (2024) 109759.
[9] N.S. Jakubovics, S.D. Goodman, L. Mashburn-Warren, et al., Periodontol. 2000 86 (2021) 32–56.
[10] Y. Cai, M. Qiao, X. Xie, et al., Chem. Eng. J. 505 (2025) 159665.
[11] Y.J. Yu, J.H. Yan, Q.W. Chen, et al., J. Control. Release 353 (2023) 591–610.
[12] A. Zhang, H. Wu, X. Chen, et al., Sci. Adv. (2023) eadg9116.
[13] X. Yuan, J.-L. Zhou, L. Yuan, et al., Sci. China Chem. 68 (2024) 826–865.
[14] M. Lu, S. Li, Y. Liu, et al., Nano Today 57 (2024) 102327.
[15] G. Wei, G. Yang, Y. Wang, et al., Theranostics 10 (2020) 12241–12262.
[16] V.N. Nguyen, Z. Zhao, B.Z. Tang, et al., Chem. Soc. Rev. 51 (2022) 3324–3340.
[17] Y. Chen, Y. Gao, Y. Chen, et al., J. Control. Release 328 (2020) 251–262.
[18] Q. Wu, J. Liu, H. Wang, et al., Chem. Eng. J. 502 (2024) 158128.
[19] Y. Zhang, L. Yang, J. jiao, et al., Adv. Sci. 12 (2025) e01501.
[20] X. Hu, H. Zhang, Y. Wang, et al., Chem. Eng. J. 450 (2022) 138129.
[21] Y. Zhu, M. Gao, M. Su, et al., Angew. Chem. Int. Ed. 62 (2023) e202306803.
[22] B. Yuan, H. Wu, H. Wang, et al., Angew. Chem. Int. Ed. 60 (2021) 706–710.
[23] M. Xu, S. Yu, P. Li, et al., J. Control. Release 378 (2025) 588–604.
[24] Q. Guo, S. Xue, J. Feng, et al., Adv. Healthc. Mater. 12 (2023) e2300818.
[25] Y. Ma, X. Zhao, P. Tian, et al., Small 20 (2024) e2306402.
[26] Y. Huang, J. Li, Z. Yu, et al., Adv. Mater. 36 (2024) e2414111.
[27] S. Guo, D. Gu, Y. Yang, J. Tian, X. Chen, J. Nanobiotechnology 21 (2023) 348.
[28] X. Duan, J. Li, S. Huang, et al., Chem. Eng. J. 477 (2023) 146937.
[29] X. Wu, M. Qi, C. Liu, et al., Theranostics 13 (2023) 2350–2367.
[30] X. Cai, J. Tian, J. Zhu, et al., Chem. Eng. J. 426 (2021) 131919.
[31] X. Huang, Y. Fu, Y. Guo, et al., Chem. Eng. J. 481 (2024) 148649.
[32] J. Song, W. Liu, L. Yang, et al., Adv. Healthc. Mater. 14 (2025) e2500987.
[33] L. Fang, Z. Chen, J. Dai, et al., Adv. Sci. 12 (2025) e2409157.
[34] C. Wang, S. Lv, Z. Sun, et al., Aggregate 5 (2024) e587.
[35] J. Wang, Q. Gong, L. Jiao, E. Hao, Coord. Chem. Rev. 496 (2023) 215367.
[36] L. Yang, S. Song, M. Yin, et al., Asian J. Pharm Sci. 18 (2023) 100810.
[37] Z. Wang, X. Liu, Y. Duan, et al., Biomaterials 280 (2022) 121249.
[38] Z. Wang, X. Liu, Y. Duan, Y. Huang, Nat. Commun. 14 (2023) 7251.
[39] Y. Zhang, T. Yue, W. Gu, et al., J. Nanobiotechnology 2 (2022) 55.
[40] L. Xu, B. Lu, K. Xie, et al., Adv. Healthc. Mater. 14 (2025) e2403318.
[41] X. Yu, J. Zhao, X. Ma, et al., Chem. Eng. J. 465 (2023) 142933.
[42] M. Qin, X. Zhang, H. Ding, et al., Adv. Mater. 36 (2024) e2402530.
[43] A. Antonoplis, X. Zang, M.A. Huttner, et al., J. Am. Chem. Soc. 140 (2018) 16140–16151.
[44] J. Xie, M. Zhou, Y. Qian, et al., Nat. Commun. 12 (2021) 5898.
[45] H. Liu, L. Tang, Y. Yin, et al., Adv. Sci. 11 (2024) e2403101.
[46] J. Jiang, D. Yang, X. Lv, et al., Adv. Funct. Mater. 35 (2025) 07540.
[47] W. Wang, W. Xu, J. Zhang, et al., ACS Nano 18 (2024) 4089–4103.
[48] N. Ding, B. Zhang, I.M. Khan, et al., ACS Appl. Mater. 16 (2024) 30728–30741.
[49] Q.S. Deng, Y. Gao, B.Y. Rui, et al., Bioact. Mater. 27 (2023) 409–428.
[50] X. Huang, Z. Shen, Q. Deng, et al., Chem. Eng. J. 505 (2025) 159380.
[51] H. Hu, S.Y. Hua, X. Lin, et al., ACS Nano 17 (2023) 11692–11712.
[52] X. Lin, J. He, W. Li, et al., ACS Nano 15 (2021) 16625–16641.
[53] J. Wei, X. Zhang, B. Sui, et al., ACS Nano 19 (2025) 11807–11822.